Faceting of a growing crystal surface by surface diffusion

T. V. Savina, A. A. Golovin, and S. H. Davis
Department of Engineering Sciences and Applied Mathematics, Northwestern University, Evanston, Illinois 60208-3100

A. A. Nepomnyashchy
Department of Mathematics, Technion—Israel Institute of Technology, Haifa 32000, Israel
and Minerva Center for Nonlinear Physics of Complex Systems, Technion—Israel Institute of Technology, Haifa 32000, Israel

P. W. Voorhees
Department of Materials Sciences and Engineering, Northwestern University, Evanston, Illinois 60208-3100
(Received 29 September 2002; published 26 February 2003)

Consider faceting of a crystal surface caused by strongly anisotropic surface tension, driven by surface diffusion and accompanied by deposition (etching) due to fluxes normal to the surface. Nonlinear evolution equations describing the faceting of $1+1$ and $2+1$ crystal surfaces are studied analytically, by means of matched asymptotic expansions for small growth rates, and numerically otherwise. Stationary shapes and dynamics of faceted pyramidal structures are found as functions of the growth rate. In the $1+1$ case it is shown that a solitary hill as well as periodic hill-and-valley solutions are unique, while solutions in the form of a solitary valley form a one-parameter family. It is found that with the increase of the growth rate, the faceting dynamics exhibits transitions from the power-law coarsening to the formation of pyramidal structures with a fixed average size and finally to spatiotemporally chaotic surfaces resembling the kinetic roughening.

DOI: 10.1103/PhysRevE.67.021606 PACS number(s): 68.35.Rh, 68.35.Fx

I. INTRODUCTION

Formation of pyramidal structures on growing crystal surfaces is an important phenomenon that has been attracting wide attention due in part to its role in the self-organized evolution of quantum dots [1]. In epitaxially grown solid films, these structures can develop either due to the release of elastic stresses caused by the lattice mismatch between the film and the substrate [1–3], or due to anisotropic surface fluxes caused by the Schwöbel effect [4,5]. Also, they can result from thermodynamic instability of a growing crystal surface that undergoes spinodal decomposition into faceted pyramidal structures with stable orientations [6–9]. In all the cases, the surface-tension anisotropy plays the crucial role and the main mechanism of the surface relaxation leading to the formation of surface structures is surface diffusion.

Faceting (spinodal decomposition) of thermodynamically unstable crystal surfaces caused by strongly anisotropic surface tension and driven by surface diffusion was considered in Refs. [6,7] where equilibrium slopes of the pyramidal structures as well as the coarsening rates were obtained. When a crystal surface is growing, both the equilibrium slopes of the pyramidal structures and their coarsening dynamics can substantially change depending on the growth rate, as was shown for the evaporation-condensation growth mechanism in Refs. [9–11]. In particular, in the presence of growth, the coarsening rate can become unusually fast [9,11,12]. With the increase of the growth rate, one observes a transition from pyramidal structures with specific symmetries to spatiotemporally chaotic interfaces [11].

When modeling the surface-tension-anisotropy-induced faceting of a crystal surface within the continuum framework, the corresponding evolution equations are ill posed (there is no short-wave cutoff) unless the additional energy of edges and corners is included. This in turn leads to the dependence of surface tension on the local curvature [6,8,10].

In the present paper, we investigate the formation of faceted pyramidal structures caused by strongly anisotropic surface tension and driven by the surface-diffusion mechanism in the case when the crystal is growing. Two types of crystal growth should be distinguished. In one type, typical of molecular-beam epitaxy, there is a constant vertical flux of material onto the surface so that there is a mean surface growth velocity. In the frame of reference moving with this velocity the surface dynamics is *not* affected by the growth and is completely described by the surface-diffusion equations that take into account the surface-tension anisotropy [6,7]. In the second type, typical of chemical-vapor deposition, the flux of material on a growing crystal surface is from the diffusion boundary layer whose shape follows the shape of the surface. In this case, the material flux is *normal* to the surface, similar to the evaporation-condensation growth mechanism considered in Refs. [9,11].

In the latter case, the corresponding evolution equation describing the surface dynamics contains an additional, symmetry-breaking convective term that describes the effect of the normal growth and significantly changes the surface dynamics [9,11,12] making it dependent on the growth rate. The interplay between the surface-tension-anisotropy-induced faceting and the surface growth by a normal flux is the main subject of the present paper.

II. MATHEMATICAL MODEL

We consider a growing surface of a crystal with cubic symmetry and anisotropic surface tension γ depending on

the surface orientation $\mathbf{n}$ and the local mean curvature $\mathcal{K}$ as [9]

$$\gamma=\gamma_0[1+\epsilon_4(n_x^4+n_y^4+n_z^4)+\epsilon_6(n_x^6+n_y^6+n_z^6)+\cdots]+\frac{1}{2}\nu\mathcal{K}^2, \tag{1}$$

where ϵ_4 and ϵ_6 are anisotropy coefficients and ν is the regularization coefficient induced by edge energies. We assume that the crystal is growing due to a constant *normal* flux F of the material, which is adsorbed on the surface and is redistributed by surface diffusion. Following Refs. [13,14] (see also Ref. [15]), a phenomenological equation describing evolution of the surface given by $z=h(x,y,t)$ can be written as

$$v_n=\frac{h_t}{\sqrt{1+(\nabla h)^2}}=F-\frac{D_s\Omega^2\sigma}{kT}\nabla_s^2\mu, \tag{2}$$

where v_n is the normal growth rate, D_s is the surface diffusivity of the adatoms, Ω is the atomic volume, σ is the surface density of atoms, k is the Boltzmann constant, T is the absolute temperature, ∇_s^2 is the surface Laplacian operator, μ is the surface chemical potential,

$$\mu=\frac{\delta\mathcal{F}}{\delta h}, \tag{3}$$

and $\mathcal{F}$ is the surface free energy,

$$\mathcal{F}=\int\gamma(\mathbf{n},\mathcal{K})dS. \tag{4}$$

We employ a long-wave approximation and expand Eq. (2) in the powers of the surface slope to obtain the following evolution equation for the surface shape in the frame moving with the surface in the z direction:

$$h_t=\frac{1}{2}F|\nabla h|^2-N\nabla^2[(-m+\alpha h_x^2+\beta h_y^2)h_{xx}+(-m+\beta h_x^2+\alpha h_y^2)h_{yy}+ch_xh_yh_{xy}-\delta\nabla^4h], \tag{5}$$

where $N=D_s\Omega^2\sigma\gamma_0/(kT)$, $\delta=\nu/\gamma_0>0$, and the coefficients m, α, β, c can be expressed in terms of the anisotropy coefficients ϵ_4, ϵ_6; see Ref. [9] for details. In the derivation of Eq. (5) we have neglected all nonlinear terms in the surface Laplacian operator as well as in the regularization terms.

Note that one should be cautious when using the long-wave expansion of the original problem (2). When there is no deposition, $F=0$, the original Eq. (2) has a Lyapunov functional, $\mathcal{L}(\nabla h,\nabla^2h)$, that satisfies the condition $\partial_t\mathcal{L}\leqslant 0$, and therefore Eq. (2) describes the relaxational (potential) dynamics in which the surface shape is gradually tending to the equilibrium configuration. This important property, however, can be lost when one approximates Eq. (2) by taking into account some long-wave terms and neglecting the others. In order for the long-wave approximation (5) to be physically meaningful, this equation, for $F=0$, must have the form

$$h_t=\nabla^2\frac{\delta\mathcal{L}}{\delta h}. \tag{6}$$

It is easy to check that for $F=0$, Eq. (5) can be written in the form (6) if $c=4\beta$. In this case, $\mathcal{L}=N\int\Phi\,dx\,dy$, where

$$\Phi=-\frac{m}{2}(\nabla h)^2+\frac{\delta}{2}(\nabla^2h)^2+\frac{\alpha}{12}(h_x^4+h_y^4)+\frac{\beta}{2}h_x^2h_y^2. \tag{7}$$

Therefore, we shall further consider Eq. (5) with $c=4\beta$:

$$h_t=\frac{F}{2}|\nabla h|^2-N\nabla^2[(-m+\alpha h_x^2+\beta h_y^2)h_{xx}+(-m+\beta h_x^2+\alpha h_y^2)h_{yy}+4\beta h_xh_yh_{xy}-\delta\nabla^4h]. \tag{8}$$

Equation (8) is invariant with respect to transformations $x\leftrightarrow -x$, $y\leftrightarrow -y$, and $x\leftrightarrow y$. This reflects the fourfold symmetry of the [001] surface. Also, after coordinate rotation by $\pm\pi/4$ it is transformed into the same equation but with different coefficients, $\tilde{\alpha}$ and $\tilde{\beta}$, that are related to the old coefficients by $\tilde{\alpha}=(\alpha+3\beta)/2$, $\tilde{\beta}=(\alpha-\beta)/2$.

We consider the coefficients α and β to be positive, since otherwise the corresponding nonlinear terms will become destabilizing and will not describe the nonlinear saturation of the surface slope (this drawback is the consequence of the long-wave approximation and in principle can be eliminated by taking into account higher-order terms in the long-wave expansions, but we shall not discuss that situation). Also, the nonlinear terms should be such that no finite slope of the surface ($h_x=A$, $h_y=B$) can make the nonlinear terms destabilizing (otherwise it will lead to an unlimited growth and the problem will become ill posed). This requirement is equivalent to the condition of the positive definiteness of the quadratic form

$$Q_{AB}(k_x,k_y)=(\alpha A^2+\beta B^2)k_x^2+(\beta A^2+\alpha B^2)k_y^2+4\beta ABk_xk_y>0, \tag{9}$$

which is obtained if one considers linear stability of a planar surface $h=Ax+By$ with respect to perturbations $\tilde{h}\sim\exp[\sigma t+i\mathbf{k}\cdot\mathbf{r}]$, where $\mathbf{k}=(k_x,k_y)$. Condition (9) leads to the following simple restriction for the coefficients α and β:

$$\alpha\geqslant\beta. \tag{10}$$

Note that this condition coincides with the positiveness of the nonlinear coefficients in the equation obtained from Eq. (5) after coordinate rotation by 45°.

By rescaling $\mathbf{r}\rightarrow\mathbf{r}\sqrt{\delta/m}$, $t\rightarrow t\delta^2/(Nm^3)$, $h\rightarrow h\sqrt{3\delta/\alpha}$, Eq. (5) can be conveniently written as

$$h_t=\frac{1}{2}D|\nabla h|^2+\nabla^2[\nabla^2 h+\nabla^4 h-(3h_x^2+bh_y^2)h_{xx}-(3h_y^2+bh_x^2)h_{yy}-4bh_x h_y h_{xy}], \quad (11)$$

where $b=3\beta/\alpha$, and $D=F\sqrt{3\delta^3}/(Nm^2\alpha^{1/2})$.

Equation (11) describes evolution in the presence of the normal growth of thermodynamically unstable crystal surface caused by the surface-tension anisotropy and driven by surface diffusion. The first term on the right-hand side is the typical KPZ-type (Kardar-Parisi-Zhang) nonlinearity caused by the normal growth [16]. The coefficient D is proportional to the growth rate F. The second term on the right-hand side describes the reconstruction of the surface by means of surface diffusion with the linear terms, $\nabla^4 h$ and $\nabla^6 h$, corresponding to the spinodal instability and the regularizing effect of the additional energy of edges and corners, respectively, while the nonlinear terms are related to the nonlinear stabilization of the anisotropic surface tension that selects stable orientations of pyramidal structures [9]. Equation (11) is similar to that studied in Ref. [9] for the case of a thermodynamically unstable surface growing by the evaporation-condensation mechanism, but contains the higher spatial derivatives associated with the surface-diffusion mechanism. Also, similar equations (however, without the KPZ nonlinearity term) were considered in Refs. [6,7] for the faceting of thermodynamically unstable surfaces by both evaporation-condensation and surface-diffusion mechanisms, as well as for the anisotropic mound formation in molecular-beam epitaxy caused by anisotropic surface currents [4,5].

III. 1+1 MODEL

We first consider a model $1+1$ case corresponding to a two-dimensional crystal with a one-dimensional surface. In this case, Eq. (11) can be rewritten for the surface slope, $u=h_x$, as

$$u_t=(u_{xx}+u-u^3)_{xxxx}+Duu_x. \quad (12)$$

Equation (12) is a higher-order convective Cahn-Hilliard equation similar to the equation considered in Ref. [17] for the dynamics of driven phase-separating systems and in Ref. [11] for the faceting of a crystal surface growing by evaporation-condensation mechanism. However, it contains the higher spatial derivatives associated with the surface diffusion.

A. Stationary surface shapes: A hill or a valley

First we study stationary surface shapes described by Eq. (12) and consider the analytically tractable case with $D=\varepsilon \ll 1$ corresponding to a small deposition rate. For $D=0$ Eq. (12) has stationary solutions

$$u_0(x)=\pm\tanh(x/\sqrt{2}), \quad (13)$$

corresponding to the surface shapes $h_0(x)=\pm\sqrt{2}\ln\cosh(x/\sqrt{2})$ that describe a hill $(-)$ or a valley $(+)$ with a unit slope. Below, we shall call the solution $u_0^+(x)=\tanh(x/\sqrt{2})$ a kink, and the solution $u_0^-(x)=-\tanh(x/\sqrt{2})$ an antikink.

For $D=\varepsilon \ll 1$, stationary solutions of Eq. (12) can be approximately found using the method of matched asymptotic expansions. Since Eq. (12) is invariant with respect to transformation $u\to -u$, $x\to -x$, we seek stationary solutions, odd about the origin, bounded at infinity and, since Eq. (12) is invariant with respect to transformation $\varepsilon\to-\varepsilon$, $u\to -u$, we take $\varepsilon>0$ (the case $\varepsilon<0$ corresponds to the withdrawal of the material from the surface, i.e., to the surface etching).

The stationary version of Eq. (12) can be integrated once to give a fifth-order differential equation

$$(u_{xx}+u-u^3)_{xxx}+\frac{\varepsilon}{2}(u^2-A^2)=0, \quad (14)$$

where the integration constant $\varepsilon A^2/2=\varepsilon u^2(\pm\infty)/2$, allowing that $u(x)$ tends to a constant value at infinity.

A unique solution to this equation requires six conditions (since the constant A is unknown). For odd solutions, $u(0)=u_{xx}(0)=u_{xxxx}(0)=0$. For solutions $u(x)$ bounded at infinity and such that $u(x)\to u_0(x)$ for $\varepsilon\to 0$, the remaining three conditions should be, for example,

$$u'(0)=u_0'(0)+z_1, \quad u'''(0)=u_0'''(0)+z_2, \quad A=\pm 1+z_3, \quad (15)$$

where z_1, z_2, and z_3 are small arbitrary constants such that $z_i\to 0$ for $\varepsilon\to 0$ and the prime corresponds to a derivative with respect to x.

In order to find these constants we examine the solutions for large x following the analysis carried out in Ref. [17] for a driven Cahn-Hilliard equation. Linearize Eq. (14) around the value A for large positive x, $u(x)=A+U(x)$, which gives

$$[U_{xx}+(1-3A^2)U]_{xxx}+\varepsilon AU=0. \quad (16)$$

The general solution of this homogeneous equation is

$$U=\sum_{i=1}^{5} a_i \exp\sigma_i x, \quad (17)$$

where σ_i are the roots of the equation

$$\sigma^5+(1-3A^2)\sigma^3+\varepsilon A=0. \quad (18)$$

For $U(x)$ to be small as $x\to+\infty$ $(x\to-\infty)$, the coefficients a_i, corresponding to the eigenvalues σ_i with positive (negative) real part, must vanish.

Let us compare the number of such roots with the number, 3, of arbitrary parameters z_i [see Eq. (15)]. Take $x\to+\infty$, so that $A>0$ for a kink, and $A<0$ for an antikink.

(a) If $3A^2-1>0$, $A>0$, the roots of Eq. (18) have the following asymptotics for $\varepsilon\ll 1$:

$$\sigma_1=+\sqrt{3A^2-1}+\cdots, \quad \sigma_2=-\sqrt{3A^2-1}+\cdots, \quad (19)$$

$$\sigma_3=\varepsilon^{1/3}[A/(3A^2-1)]^{1/3}+\cdots, \tag{20}$$

$$\sigma_{4,5}=\varepsilon^{1/3}[A/(3A^2-1)]^{1/3}(-1/2\pm i\sqrt{3}/2)+\cdots. \tag{21}$$

This situation corresponds to a kink whose principal part coincides with $u_0=\tanh(x/\sqrt{2})$ for $x=O(1)$, and has small oscillations for $x=O(\varepsilon^{-1/3})$. In this case, there are two roots with positive real part.

(b) If $3A^2-1>0$, $A<0$, asymptotics for the roots are

$$\sigma_1=+\sqrt{3A^2-1}+\cdots, \quad \sigma_2=-\sqrt{3A^2-1}+\cdots, \tag{22}$$

$$\sigma_3=-\varepsilon^{1/3}[|A|/(3A^2-1)]^{1/3}+\cdots, \tag{23}$$

$$\sigma_{4,5}=\varepsilon^{1/3}[|A|/(3A^2-1)]^{1/3}(1/2\pm i\sqrt{3}/2)+\cdots. \tag{24}$$

This situation corresponds to an antikink whose principal part coincides with $u_0=-\tanh(x/\sqrt{2})$ for $x=O(1)$. In this case, there are no oscillations for $x=O(\varepsilon^{-1/3})$ and there are three roots with positive real parts.

(c) If $3A^2-1<0$, $A>0$, then

$$\sigma_{1,2}=\pm i\sqrt{1-3A^2}-\varepsilon A/[2(1-3A^2)^2]+\cdots, \tag{25}$$

$$\sigma_3=-\varepsilon^{1/3}[A/(1-3A^2)]^{1/3}+\cdots, \tag{26}$$

$$\sigma_{4,5}=\varepsilon^{1/3}[A/(1-3A^2)]^{1/3}(1/2\pm i\sqrt{3}/2)+\cdots, \tag{27}$$

and there are two roots with positive real parts.

(d) $3A^2-1<0$, $A<0$,

$$\sigma_{1,2}=\pm i\sqrt{1-3A^2}+\varepsilon|A|/[2(1-3A^2)^2]+\cdots, \tag{28}$$

$$\sigma_3=\varepsilon^{1/3}[|A|/(1-3A^2)]^{1/3}+\cdots, \tag{29}$$

$$\sigma_{4,5}=\varepsilon^{1/3}[|A|/(1-3A^2)]^{1/3}(-1/2\pm i\sqrt{3}/2)+\cdots, \tag{30}$$

and there are three roots with positive real parts.

Solutions corresponding to the cases (c) and (d) oscillate near $x=0$ and are of no interest here since they do not describe appropriate surface shapes in the form of a hill or a valley. Comparing cases (a) and (b), one can see that the positive and negative kinks are intrinsically different. The dimension of the stable manifold near the stationary point $|A|$ is equal to 3, while the dimension of the unstable manifold near this point is 2. On the other hand, in the neighborhood of the stationary point $-|A|$, the dimensions of the stable and unstable manifolds are 2 and 3, respectively. Since for a negative kink the number of roots with positive real parts is equal to the number of arbitrary parameters, the negative kink is unique (if exists), while for a positive kink one can expect a one-parameter family of solutions. In order to find these solutions we apply the method of matched asymptotic expansions with the short-scale variable x and the long-scale variable $\xi=\varepsilon^{1/3}x$ [see Eq. (17) with Eqs. (21) and (23)].

1. Inner solution

Look for the inner solution of the equation

$$(u_{xx}+u-u^3)_{xxx}+\frac{\varepsilon}{2}(u^2-A^2)=0 \tag{31}$$

in the form

$$u_{inner}=u_0(x)+\varepsilon^{1/3}u_1(x)+\varepsilon^{2/3}u_2(x)+\varepsilon u_3(x)+\cdots, \tag{32}$$

where the first term coincides with Eq. (13). Note that in order to obtain asymptotics for the whole Eq. (31) one has to take into account terms at least up to the order ε in expansion (32).

The unknown constant A should be expanded as well:

$$A=\pm(1+\varepsilon^{1/3}\Delta_1+\varepsilon^{2/3}\Delta_2+\varepsilon\Delta_3+\cdots). \tag{33}$$

Substituting Eqs. (32) and (33) into Eq. (31) and equating the terms of equal powers of ε, one obtains

$$(\mathcal{L}u_1)_{xxx}=0, \tag{34}$$

$$(\mathcal{L}u_2)_{xxx}=(3u_0^2u_1)_{xxx}, \tag{35}$$

$$(\mathcal{L}u_3)_{xxx}=(6u_0u_1u_2+u_1^3)_{xxx}-\frac{1}{2}(u_0^2-1), \tag{36}$$

where $\mathcal{L}=d^2/dx^2+(1-3u_0^2)$.

Integrating Eqs. (34)–(36) three times and taking into account that the solutions must be odd functions of x, one obtains

$$\mathcal{L}u_i=g_i(x), \tag{37}$$

where

$$g_1(x)=C_1x, \qquad g_2(x)=(3u_0^2u_1)+C_2x, \tag{38}$$

$$g_3(x)=6u_0u_1u_2+u_1^3+f(x)+C_3x, \tag{39}$$

C_1, C_2, and C_3 are arbitrary constants,

$$f(x)=-\frac{\sqrt{2}}{2}\mathrm{dilog}(\exp(x\sqrt{2})+1)-\frac{\sqrt{2}}{4}x^2-\frac{\sqrt{2}}{24}\pi^2, \tag{40}$$

and

$$\mathrm{dilog}(x)=\int_1^x(1-t)^{-1}\ln t\,dt.$$

Solutions of Eqs. (37) are then

$$u_i=\Phi_2\int\Phi_1g_iW^{-1}dx-\Phi_1\int\Phi_2g_iW^{-1}dx, \tag{41}$$

where Φ_1 and Φ_2 form the system of fundamental solutions for the differential operator $\mathcal{L}$, and $W=\Phi_1\Phi_2'-\Phi_1'\Phi_2$ is the Wronskian of this system,

$$\Phi_1=[2\cosh(x/\sqrt{2})]^{-2}, \tag{42}$$

$$\Phi_2=2\sqrt{2}\tanh(x/\sqrt{2})[\cosh(x\sqrt{2})+4] + 6x[\cosh(x/\sqrt{2})]^{-2}. \tag{43}$$

The constants C_1, C_2, and C_3 will be found from the matching.

2. Outer solution

Let us start constructing the outer solution for Eq. (31) by introducing the long-scale variable $\xi=\varepsilon^{1/3}x$. Equation (31) can then be rewritten as

$$(\varepsilon^{2/3}U_{\xi\xi}+U-U^3)_{\xi\xi\xi}+\frac{1}{2}(U^2-A^2)=0. \tag{44}$$

Look for solutions $U(\xi)$ in the form

$$U(\xi,\varepsilon)=U_0(\xi)+\varepsilon^{1/3}U_1(\xi)+\varepsilon^{2/3}U_2(\xi)+\varepsilon U_3(\xi)+\cdots. \tag{45}$$

Note that the outer solution includes two parts: the left outer solution, U^L ($\xi<0$), and the right outer solution, U^R ($\xi>0$), which are related to each other by $U^L(-\xi)=-U^R(\xi)$. For definiteness, we shall further consider only $\xi>0$. Substitute Eqs. (45) and (33) into Eq. (44) and equate the terms of equal powers of ε to get the following equations for the functions U_i:

$$(U_0-U_0^3)_{\xi\xi\xi}+\frac{1}{2}(U_0^2-1)=0, \tag{46}$$

$$LU_i=\Delta_i+f_i, \qquad i=1,2,\ldots, \tag{47}$$

where $L=(d^3/d\xi^3)(1-3U_0^2)+U_0$, $f_1=0$, and f_i, $i=2,\ldots,$ are known functions of U_k, $k<i$. The solutions of Eqs. (46) and (47) for $i=0$, 1 are

$$U_0=\pm 1, \tag{48}$$

$$U_1=a_1\exp(\mathrm{sgn}[U_0]2^{-1/3}\xi)+\exp(-\mathrm{sgn}[U_0]2^{-4/3}\xi) \times[a_2\sin(2^{-4/3}\sqrt{3}\xi)+a_3\cos(2^{-4/3}\sqrt{3}\xi)] +\mathrm{sgn}[U_0]\Delta_1. \tag{49}$$

For a positive kink, $U_0=+1$, and one must set $a_1=0$ in order to eliminate the exponentially growing term. Coefficients a_2 and a_3 should be determined from the matching. For a negative kink, $U_0=-1$; one sets $a_2=a_3=0$, and a_1 should be defined from the matching.

3. Matching

Let us consider the matching procedure for the negative kink first, since in this case we are expecting to find all of the coefficients uniquely. The right outer solution (for $\xi>0$) is

$$U^R=-1+\varepsilon^{1/3}[a_1\exp(-2^{-1/3}\xi)-\Delta_1]+\cdots. \tag{50}$$

For the matching, replace ξ by $x\varepsilon^{1/3}$ and expand Eq. (50) for fixed x with respect to small ε,

$$U^R=-1+\varepsilon^{1/3}(a_1-\Delta_1)-\varepsilon^{2/3}x2^{-1/3}a_1+\varepsilon x^2 2^{-5/3}a_1 +\varepsilon x2^{-1/3}(-12a_1^2/7+a_1/14-\Delta_2-2^{-8/3})+o(\varepsilon). \tag{51}$$

In the inner solution, one needs the asymptotics of functions u_i, $i=1$, 2, 3 for $x\to+\infty$. For u_1 one has $u_1\sim -C_1x/2$. Comparing this with the second term in Eq. (51) [see also Eq. (32)] one obtains the first two matching conditions

$$C_1=0, \quad a_1-\Delta_1=0. \tag{52}$$

Thus, it follows from the matching that $u_1(x)\equiv 0$. Matching conditions corresponding to the terms of the order $\varepsilon^{2/3}$ and ε are the following:

$$-2^{-1/3}a_1=-C_2/2, \qquad 2^{-5/3}a_1=-\sqrt{2}/8, \tag{53}$$

$$2^{-1/3}(-12a_1^2/7+a_1/14-\Delta_2-2^{-8/3})=-C_3/2, \tag{54}$$

since for $x\to+\infty$, $u_2\sim -C_2x/2$, $u_3\sim-\sqrt{2}x^2/8-C_3x/2$. From Eqs. (52) and (53) one gets $a_1=-2^{-5/6}$, $C_2=-2^{-1/6}$, and $\Delta_1=-2^{-5/6}$. Therefore,

$$A=-1+\varepsilon^{1/3}2^{-5/6}+o(\varepsilon^{1/3}). \tag{55}$$

Note that the constant C_3 cannot be determined at this step, since Δ_2 is still unknown. In order to determine these constants one has to add $\varepsilon^{4/3}u_4(x)$ to the inner solution (32) and compare the terms of the order $\varepsilon^{4/3}$. From this, one gets $C_3=(96+4\times 2^{5/6}-69\times 2^{1/3}-4\times 2^{1/6})/56\approx 0.21$, $\Delta_2=(34\times 2^{1/3}+4\times 2^{1/6}-69\times 2^{2/3}-4\sqrt{2})/112\approx -0.61$, and

$$A=-1+\varepsilon^{1/3}2^{-5/6}-\varepsilon^{2/3}(34\times 2^{1/3}+4\times 2^{1/6}-69\times 2^{2/3} -4\sqrt{2})/112+o(\varepsilon^{2/3})\approx -1+0.561\varepsilon^{1/3}+0.606\varepsilon^{2/3}. \tag{56}$$

4. Effect of the growth rate

We have obtained approximate stationary solutions of Eq. (12) describing a stationary hill or valley on a $1+1$ surface growing due to a normal flux and relaxation by surface diffusion. The main result of the analysis presented above is that a solitary hill (antikink) is unique and its slope depends on the deposition rate, D. For small $D=\varepsilon\ll 1$ the dependence is given by the asymptotic formula (56). At the same time, a solitary valley is not unique and there is a one-parameter family of valley (kink) stationary solutions with different slopes. This situation is analogous to that described in Ref. [17] for a convective Cahn-Hilliard equation of the lower order for phase separation in driven systems, which also governs the faceting of a thermodynamically unstable crystal surface growing by the evaporation-condensation mechanism [11]. Also, in a periodic structure of hills and valleys the slopes of both hills and valleys (antikinks and kinks) are defined uniquely (see the following section). The

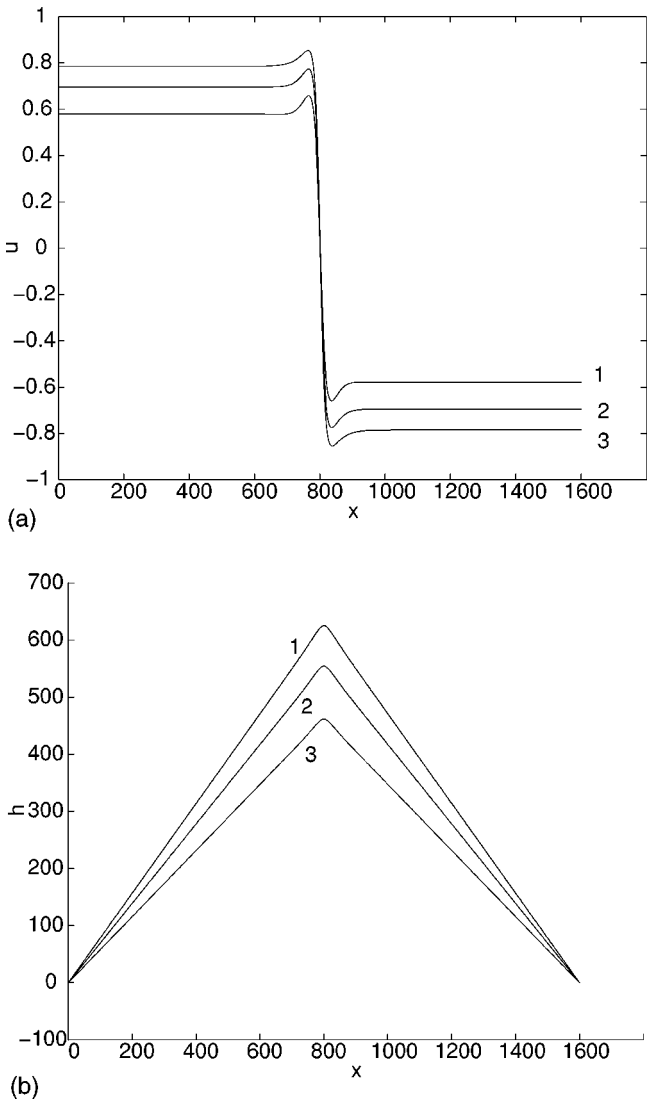

FIG. 1. Negative kinks (a) and the corresponding hills (b). Curves 1, 2, and 3 correspond to $\varepsilon=0.05$, $\varepsilon=0.1$, and $\varepsilon=0.2$, respectively.

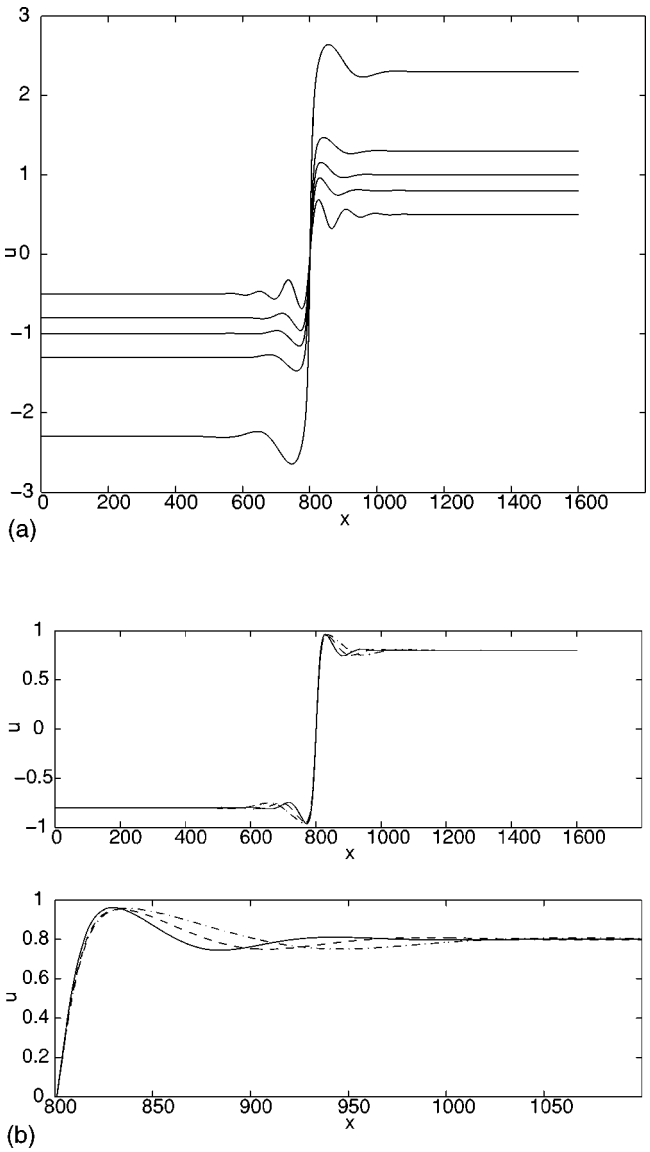

FIG. 2. (a) Family of positive kinks for fixed $\varepsilon=0.3$. (b) Family of positive kinks for fixed $A=0.8$: the solid curve corresponds to $\varepsilon=0.3$, the dashed curve corresponds to $\varepsilon=0.1$, the dashed-dotted curve corresponds to $\varepsilon=0.03$. The lower figure is the enlargement of the middle one.

dependence of the hill slope on the deposition rate D and the nonuniqueness of a kink solution corresponding to a valley are illustrated by Figs. 1 and 2, respectively. The figures show the finite-difference numerical solutions of Eq. (12) that we performed in a large domain, with the boundary conditions $u_x=u_{xxx}=u_{xxxxx}=0$ on both ends of the interval. Note that even in the case when the dimensionless deposition rate D is small it significantly affects the shape of the surface structures since the slope correction is proportional to $D^{1/3}$. When the deposition rate grows above some critical value, the surface slope decreases below the spinodal one and the surface becomes unstable. One can estimate the critical value of the parameter D using the asymptotic formulas (55) and (56). Substitute the perturbed slope $u=A+\tilde{a}\exp(\sigma t+ikx)$ in Eq. (12) to obtain the characteristic equation

$$\sigma=-k^6+k^4(1-3A^2)+i\varepsilon Ak, \tag{57}$$

from which one concludes that the instability occurs for $|A|<1/\sqrt{3}$. From Eq. (55) one gets the estimate for the stability threshold value of ε as $\varepsilon\approx 0.43$, while from Eq. (56) the estimated threshold is 0.12. Numerical simulations give a value between them, $\varepsilon\approx 0.2$, corresponding to $|A|=1/\sqrt{3}$.

B. Stationary surface shapes: Periodic array of hills and valleys

Using asymptotic solutions obtained above, we now construct a unique periodic stationary solution of Eq. (12) that will correspond to a periodic hill-and-valley structure on a growing crystal surface. For a period $2L$, this solution is schematically shown in Fig. 3. Since it is symmetric with respect to the center $(x=L,\ u=0)$, the solution $u(x)$ needs to be specified on the interval $(0,\ L)$ only.

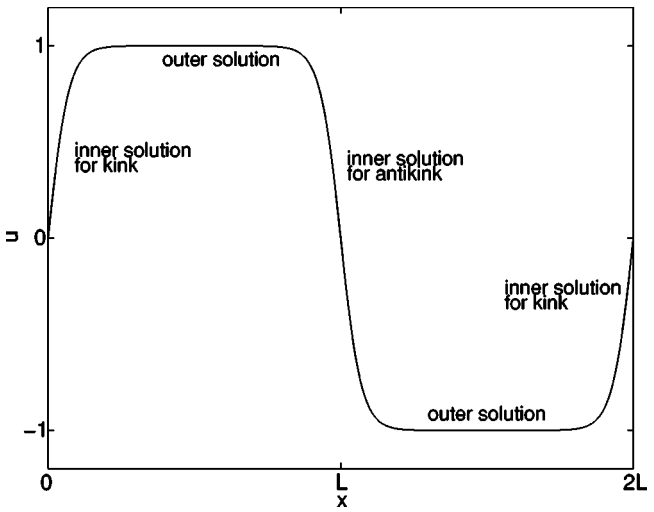

FIG. 3. The scheme of a periodic solution of Eq. (14) in the form of kink-antikink pairs.

As follows from Eqs. (48) and (49), the outer solution has the form

$$U=1+\varepsilon^{1/3}\{\Delta_1+a_1\ \exp[(\varepsilon/2)^{1/3}x]+\exp(-2^{-4/3}\varepsilon^{1/3}x)\times[a_2\ \sin(\sqrt{3}\,2^{-4/3}\varepsilon^{1/3}x)+a_3\ \cos(\sqrt{3}\,2^{-4/3}\varepsilon^{1/3}x)]\}+\cdots. \tag{58}$$

It is convenient to rewrite Eq. (58) as

$$U=1+\varepsilon^{1/3}\{\Delta_1+a_1\ \exp[l]\exp[(\varepsilon/2)^{1/3}(x-L)]+a^*\ \exp[(-1/2+i\sqrt{3}/2)l]\times\exp[2^{-4/3}\varepsilon^{1/3}(-1+i\sqrt{3})(x-L)]+a\ \exp[(-1/2-i\sqrt{3}/2)l]\times\exp[2^{-4/3}\varepsilon^{1/3}(-1-i\sqrt{3})(x-L)]\}+\cdots, \tag{59}$$

where $a^*=(a_3-ia_2)/2$, $a=(a_3+ia_2)/2$, $l=(\varepsilon/2)^{1/3}L$. The coefficients a_1, a_2, a_3, and Δ_1 will be determined from the matching conditions.

The first matching equation can be obtained by expanding Eqs. (58) and (59) for $\varepsilon^{1/3}x\ll 1$ and $\varepsilon^{1/3}(x-L)\ll 1$, respectively, and equating the terms of the order $\varepsilon^{1/3}$. This gives

$$a_1[\exp(l)-1]+a_2\ \exp(-l/2)\sin(l\sqrt{3}/2)+a_3[\exp(-l/2)\cos(l\sqrt{3}/2)-1]=0. \tag{60}$$

The asymptotics for the inner solution for a positive kink for $x\gg 1$ is

$$u\sim 1-\frac{1}{2}C_p\varepsilon^{2/3}x-\frac{\sqrt{2}}{8}\varepsilon x^2, \tag{61}$$

where C_p is a constant to be determined. Matching the outer solution with the asymptotics for the inner solution (61) gives the following equations:

$$\Delta_1=-a_1-a_3, \tag{62}$$

$$C_p=-2^{-1/3}(2a_1-a_3+a_2\sqrt{3}), \tag{63}$$

$$2a_1-a_2\sqrt{3}-a_3=-2^{1/6}. \tag{64}$$

The asymptotics for the inner solution for a negative kink located at the point L (see Fig. 3) for $L-x\gg 1$ is

$$u\sim 1-\frac{1}{2}C_n\varepsilon^{2/3}(x-L)+\frac{\sqrt{2}}{8}\varepsilon(x-L)^2, \tag{65}$$

where C_n is as yet an unknown constant. Matching the outer solution with the negative kink yields

$$C_n=-2^{-1/3}[2a_1\ \exp(l)+(-a_3+a_2\sqrt{3})\times\exp(l/2)\cos(l\sqrt{3}/2)-(a_3\sqrt{3}+a_2)\times\exp(-l/2)\sin(l\sqrt{3}/2)], \tag{66}$$

$$a_1\ \exp(l)-a_2\ \exp(-l/2)\sin(l\sqrt{3}/2+\pi/3)-a_3\ \exp(-l/2)\cos(l\sqrt{3}/2+\pi/3)=2^{-5/6}. \tag{67}$$

Solving the system of linear algebraic equations (60), (64), and (67), one finds the coefficients a_1, a_2, and a_3, and after that, using the expressions (62), (63), and (66), one can find Δ_1, C_p, and C_n.

An example of the solution found above, for $L=200$ and $\varepsilon=0.001$, is shown in Fig. 4(a), with the corresponding surface shape, $h(x)$, shown in Fig. 4(b). Figure 4(c) shows the zoom of the valley region in Fig. 4(b). One can see that the slope of a hill is smaller than that of a valley. This is the consequence of the surface growth described by the convective term Duu_x in Eq. (12) (the term $Dh_x^2/2$ in the corresponding equation for the surface shape h). Due to the deposition normal to the surface, the concave parts of the surface tend to become sharper and to produce caustics while the convex parts get smoothed. The interplay between this kinematic effect and the surface-tension anisotropy, which tends to select a specific slope, leads to the asymmetry between hills and valleys and to the existence, within some interval of the deposition rate D, of stationary surface shapes.

Figure 5 shows the combined asymptotic solutions that use the four-term inner solutions (32) and (41), matched to the two-term outer solution (58), with the coefficients obtained from Eqs. (60), (62)–(64), (66), and (67) (dotted lines), together with the numerical solutions of Eq. (12) obtained by means of a pseudospectral method with periodic boundary conditions (solid lines), for two different values of the parameter D. Figure 5(a) shows the whole period and Figs. 5(b,c) give the detailed view. One can see a very good agreement between the asymptotic and numerical solutions.

Note, however, that for D sufficiently small, the described kink-antikink (hill-and-valley) periodic solution is stable only in the case when there is one kink-antikink pair in the region. In the case when there is more than one kink-antikink pair in the region, the solution is unstable with respect to coarsening that proceeds until there is one kink-antikink pair

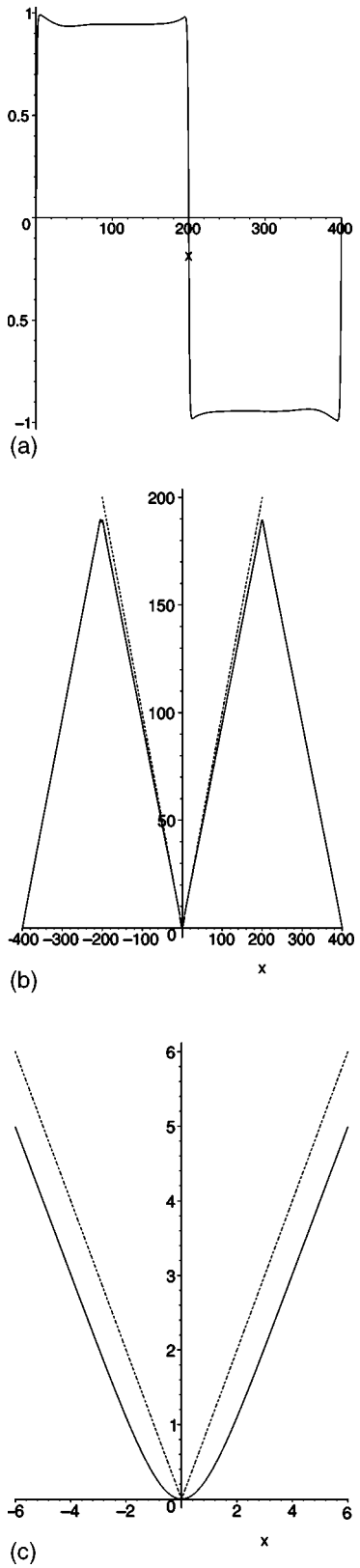

FIG. 4. (a) One period of the periodic kink-antikink solution of Eq. (14) for $L=200$ and $\varepsilon=0.001$. (b) The corresponding shape of the crystal surface (two periods); the dashed line shows the Wulff slope. (c) The zoom of the valley region in (b).

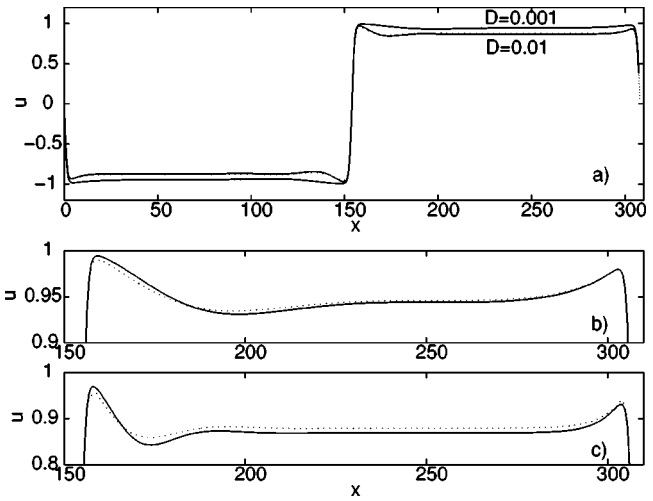

FIG. 5. (a) Surface slope $u(x)$ for two different values of the parameter D: numerical solutions of Eq. (12) by means of a pseudospectral method with periodic boundary conditions (solid lines) together with the asymptotic solutions (32), (41), and (58) (dotted lines); one can see the two solutions almost coincide. Detailed view at the numerical and asymptotic solutions shown in (a) for $D=0.001$ (b) and $D=0.01$ (c).

left. At the same time, with the increase of the deposition rate, a single kink-antikink pair in a large region becomes unstable much like a single kink or antikink in an infinite region discussed above, and exhibits transitions to a dynamic behavior. This is described in the following section.

C. Surface dynamics, coarsening, and roughening

In order to investigate the dynamics of a growing, thermodynamically unstable crystal surface that undergoes faceting by the surface-diffusion mechanism, we have performed a numerical simulation of Eq. (12) by means of a pseudospectral code, in a large domain ($L=80\pi$) with

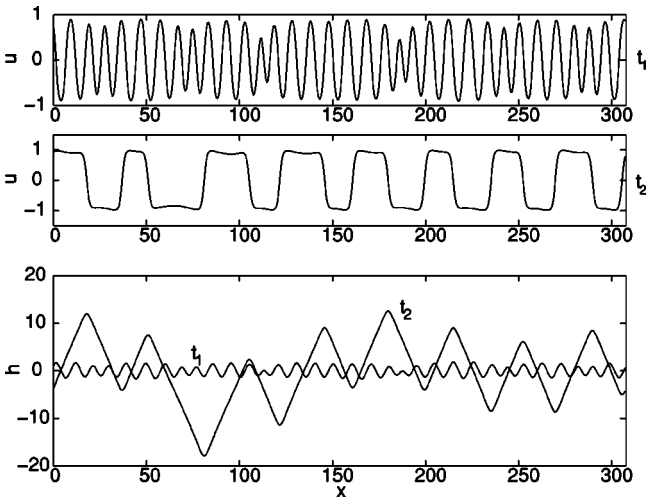

FIG. 6. Surface slope $u(x)$ and the corresponding surface shape $h(x)$ at two moments of time: right after the formation of hill-and-valley structure (t_1), and at the late stage of coarsening (t_2). Numerical solution of Eq. (12) with $D=0.02$.

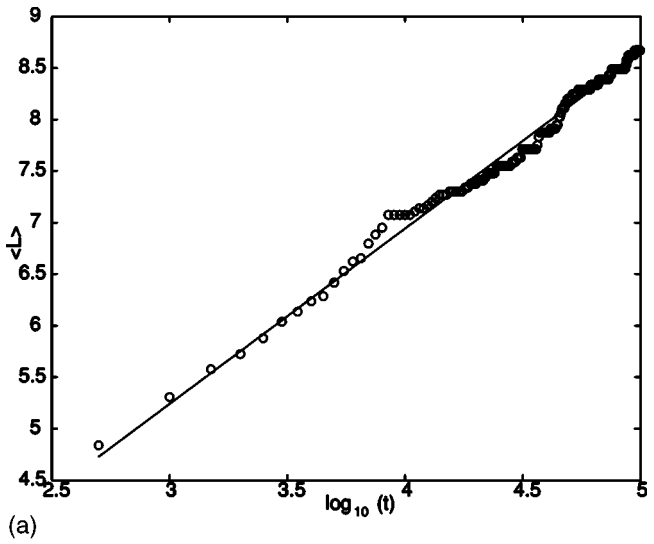

FIG. 7. (a) Coarsening kinetics for zero deposition rate, $D=0$; (b) coarsening kinetics for various values of the deposition rate: ○, $D=0.01$; □, $D=0.02$; △, $D=0.05$; ◇, $D=0.1$.

periodic boundary conditions, starting from small-amplitude random initial data. The dynamics strongly depends on the dimensionless deposition rate D. For small D we have observed the formation of a hill-and-valley structure that undergoes further coarsening. Figure 6 shows an example of the slope $u(x)$ and the surface shape $h(x)$ for $D=0.02$ at two different moments of time: at the beginning of the coarsening (t_1), when the hill-and-valley structure has been just formed with the preferred wavelength and the slope close to that of the equilibrium crystal shape without deposition, $D=0$ (Wulff slope, $u=\pm 1$), and at the late stage of coarsening (t_2). The spatial period of the initial hill-and-valley structure is determined by the balance between the corner regularization energies and the surface-tension anisotropy causing the spinodal decomposition of the planar surface. Note that once formed, the slope of hills and valleys does not change and the hill-and-valley structure coarsens in time leading to the

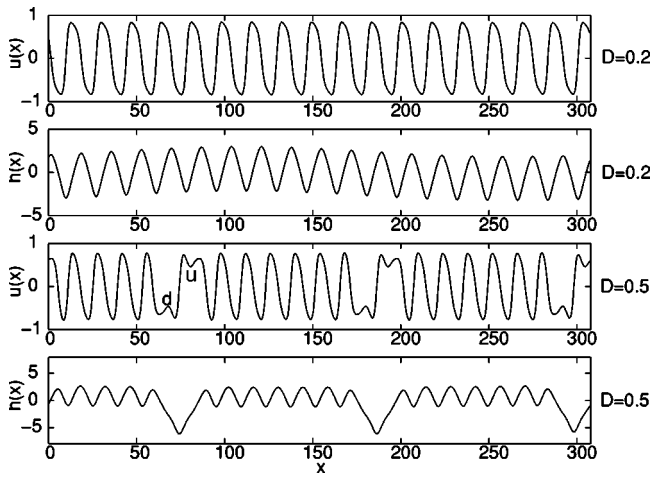

FIG. 8. Examples of stationary numerical periodic solutions of Eq. (12), and the corresponding surface shapes for two different values of the parameter D.

formation of larger hills and valleys with the same slope. For $D=0$ (no deposition, pure surface-diffusion-driven faceting) the coarsening is logarithmically slow as shown in Fig. 7(a) that presents the dependence of the mean spatial scale of the structure, $\langle L\rangle$, on time, where $\langle L\rangle$ is averaged over ten realizations with different random initial data. However, for $D>0$, no matter how small, the coarsening kinetics changes. Examples of the coarsening kinetics for different $D>0$ are given in Fig. 7(b). One can see that after the formation of a hill-and-valley structure with the preferred wave number, $k=\sqrt{2/3}$, given by the linear growth rate of the perturbations of the initial unstable state, $u=0$, the coarsening starts which consists of three stages: slow power-law coarsening, fast power-law coarsening, and extremely slow or no coarsening. One can see that with the increase of D the fast stage starts earlier, and the slow down starts earlier as well. For very small D the fast stage is probably scale invariant with $\langle L\rangle \sim t^{0.54}$. The power law at the initial slow stage should be considered as an intermediate asymptotic behavior and is not associated with scale invariance. With the increase of D (see graphs for $D=0.05$ and $D=0.1$), after the fast stage, the coarsening stops completely and one observes the formation of a stationary structure.

With further increase of the parameter D, we observe the formation of stationary or oscillating structures that do not undergo any coarsening. Some typical examples of these structures are shown in Figs. 8 and 9. Figure 8 shows two typical stationary structures. They can consist of arrays of equal or slightly modulated hills and valleys or of several hill-and-valley arrays divided by deeper valleys. These deeper valleys correspond to the pairs of ''up'' and ''down'' structures in $u(x)$ (denoted by the letters u and d in Fig. 8, respectively), the remnants of kink-antikink pairs. Similar structures were observed in the dynamics of a growing crystal surface controlled by the evaporation-condensation mechanism and described by a convective Cahn-Hilliard model studied in Ref. [11]. Selection of a particular structure depends on initial conditions and on the value of D. Figure 9 shows a typical oscillatory pattern. Here, the upper figure is

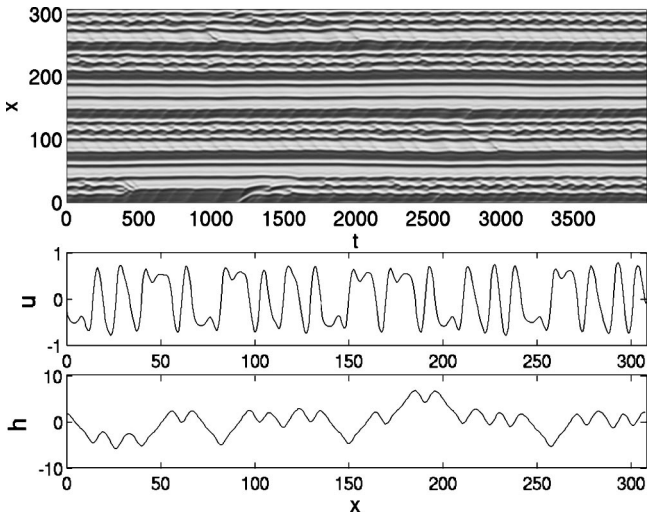

FIG. 9. Space-time diagram of the oscillating numerical solution of Eq. (12) $u(x,t)$ for $D=0.7$ (upper figure), with $u(x)$ and the corresponding $h(x)$ at a particular moment of time (lower figures).

a space-time diagram representing the oscillatory dynamics of the order parameter u. The lower figures show $u(x)$ and $h(x)$ corresponding to a particular moment of time. One can see that, similar to the structure shown in Fig. 8, there are arrays of hills and valleys divided by deeper valleys. However, here some of the hill tops exhibit spatially localized oscillations.

A further increase of the dimensionless deposition rate D leads to the transition to a chaotic spatiotemporal dynamics of the surface structures. Figure 10(a) shows spatiotemporal diagrams corresponding to the dynamics of the order parameter u for three different deposition rates. One can see that with the increase of D the chaotic component of the hill oscillations becomes more pronounced, the characteristic spatial scale decreases, and the events of splitting and merging of kinks and antikinks (valleys and hills) become more frequent. Figure 10(b) shows the surface shapes $h(x)$ corresponding to particular moments of time for different deposition rates D. One can see that for smaller D hills and valleys with a particular slope dominate, while with the increase of D the slope of hills and valleys become more and more random. In all cases there is a tendency to form a rough surface. For large D, the surface structure consists of mounds, randomly distributed in space and merging and splitting in a chaotic manner, much similar to the dynamics described by the Kuramoto-Sivashinsky equation [18]. Indeed, by the transformation $u \to u/D$, Eq. (12) is transformed to the equation

$$u_t - u u_x - u_{xxxx} - u_{xxxxxx} - \frac{1}{D}(u^3)_{xxxx} = 0, \qquad (68)$$

which, for $D \to \infty$, is reduced to a Kuramoto-Sivashinsky-type equation whose linear operator has higher derivatives. Like a Kuramoto-Sivashinsky equation, Eq. (68) with $D \to \infty$ has a Galilean invariance and exhibits chaotic spatiotemporal dynamics. The characteristic feature of this dynamics is that there is a preferred spatial scale present in the

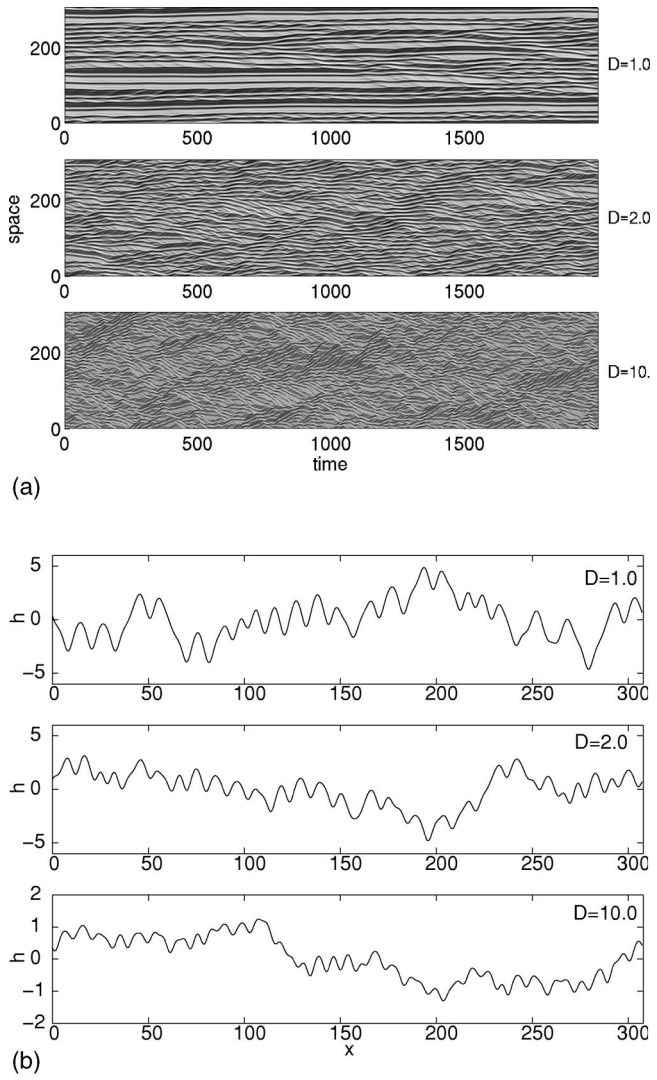

FIG. 10. (a) Space-time diagrams of nonstationary solutions of Eq. (12) $u(x,t)$ for various values of D; (b) surface shapes $h(x)$ corresponding to the nonstationary solutions of Eq. (12) $u(x,t)$ shown in (a), at a particular moment of time.

system, close to the most rapidly growing wave number given by the linear theory, $k=\sqrt{2/3}$. The time-average spatial power spectra of chaotic solutions of Eq. (68) corresponding to different values of D are shown in Fig. 11(a). These spectra are similar to those of chaotic solutions of the Kuramoto-Sivashinsky (KS) equation. One can see that the characteristic lateral scale of the surface mounds increases with the decrease of the deposition rate D. Note a characteristic shift of the spectrum in the short-wave region: it corresponds to the appearance of kink-antikink pairs divided by a boundary layer (top of a hill or bottom of a valley). A characteristic wave number at which this shift occurs, $k \approx 1.7$, corresponds to a typical width of the ''interface'' between kinks and antikinks, $\lambda = 2\pi/k \approx 3.7$. The number of kink-antikink pairs increases with the decrease of D. Note also that there is a significant input of long-wave modes corresponding to a plateau of the spatial power spectrum. One can see that the power of the long-wave modes increases with the increase of

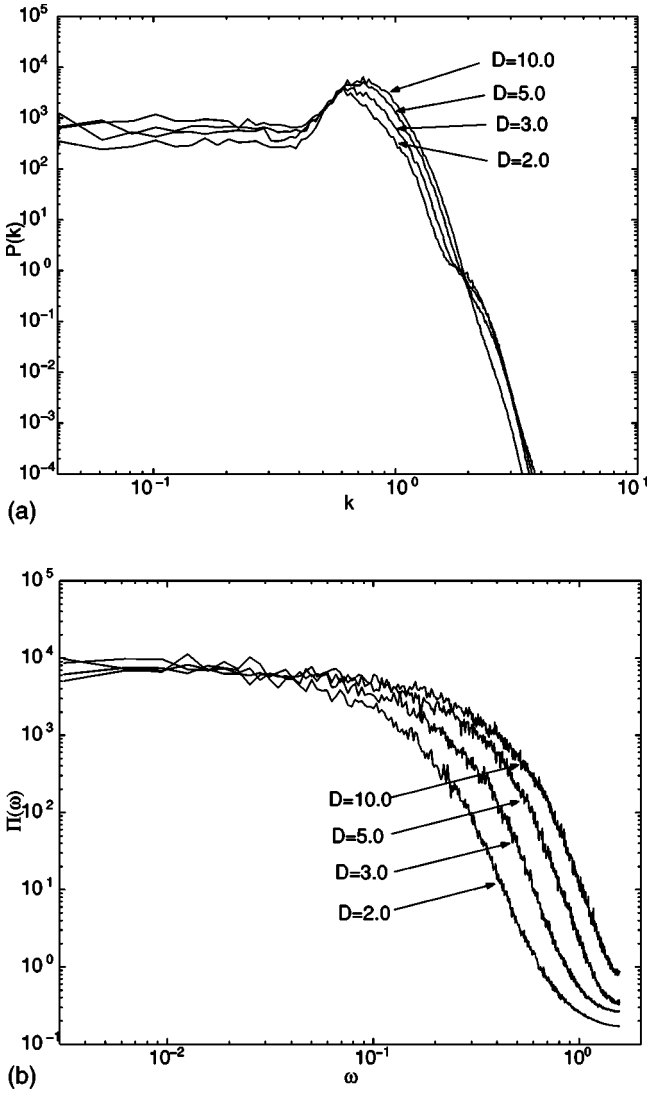

FIG. 11. (a) Time-averaged spatial power spectra $P(k)$ (k is the wave number) of chaotic solutions of Eq. (12) for various values of D. (b) Space-averaged time power spectra $\Pi(\omega)$ (ω is the frequency) of chaotic solutions of Eq. (12) for various values of D.

D. The long-wave modes are known to play a crucial role in the roughening dynamics described by the KS equation [18]. The space-averaged time power spectra of chaotic solutions of Eq. (68), corresponding to different values of D, are shown in Fig. 11(b). One can see that with the increase of the deposition rate D, the power of the high-frequency oscillations increases.

Transition from the coarsening dynamics, typical of phase-separating systems, to a chaotic spatiotemporal dynamics with the increase of the deposition rate is also observed in the convective Cahn-Hilliard models with evaporation-condensation mechanism [11]. Such behavior resembles the phenomenon of kinetic roughening [19,20]. Indeed, the KS equation describing the shape of a growing thermodynamically unstable surface for large growth rates ($D\to\infty$) exhibits roughening of the KPZ universality class [18,21]. An interesting question which remains open is what are the roughening exponents of a surface described by Eq. (68) for infinite and finite values of D in a chaotic regime. We leave this for future investigations.

IV. 2+1 MODEL

Now we consider faceting of a growing crystal surface caused by anisotropic surface tension and driven by the surface-diffusion mechanism, in a more realistic $2+1$ case corresponding to a two-dimensional surface of a three-dimensional crystal. The surface evolution, in the case of [001] surface, is described by Eq. (11). As we did for the model $1+1$ case, we first consider stationary solutions of Eq. (11) corresponding to pyramidal structures.

A. Single pyramid

Here we shall study a stationary solution of Eq. (11) in the form of a square pyramid. We will be interested in the case of a small deposition rate, $D=\varepsilon\ll 1$.

Consider a symmetric square pyramid oriented in such a way that projections of its edges on the basis plane coincide with x and y axes. Then, the pyramidal shape $h(x,y,t)$ has the following asymptotics [9]:

$$h\sim \pm Ay+f(x)+\varepsilon v t \qquad \text{as} \quad y\to\pm\infty, \tag{69}$$

$$h\sim \pm Ax+f(y)+\varepsilon v t \qquad \text{as} \quad x\to\pm\infty, \tag{70}$$

where εv is the speed of the surface growth in the z direction, $A<0$ is the slope of the pyramidal edges, and $f(x)$ is a function to be determined. From the symmetry (compare, for example, Eqs. (69) and (70) when both variables x and y tend to infinity) it follows that

$$f'(\pm\infty)=\pm A, \tag{71}$$

where the prime means a derivative.

Substitute Eq. (69) in Eq. (11) to obtain the following equation for $f(x)$:

$$[f_{xxx}+f_x(1-bA^2)-f_x^3]_{xxx}+\frac{\varepsilon}{2}f_x^2+\varepsilon\left(\frac{A^2}{2}-v\right)=0. \tag{72}$$

Since $f_x^2(\infty)=A^2$, the last term in Eq. (72) must be equal to $-\varepsilon A^2/2$ and therefore $v=A^2$. By replacing f_x by u in Eq. (72) one obtains

$$[u_{xx}+(1-bA^2)u-u^3]_{xxx}+\frac{\varepsilon}{2}(u^2-A^2)=0. \tag{73}$$

Equation (73) is similar to Eq. (14) and has an unknown coefficient $(1-bA^2)$. Here b is a given anisotropy constant in Eq. (11) and A should be determined.

For $\varepsilon=0$, Eq. (73) has the following solutions:

$$u(x)=\pm\sqrt{1-bA^2}\,\tanh[x\sqrt{(1-bA^2)/2}]. \tag{74}$$

Condition (71) yields $A^2=1-bA^2$ so that

$$A = \pm \frac{1}{\sqrt{1+b}}. \tag{75}$$

Thus, the asymptotics of the pyramid (antipyramid) for $y \to +\infty$ is

$$h \sim \mp \frac{y}{\sqrt{1+b}} \mp \sqrt{2} \ln[\cosh(x/\sqrt{2+2b})]. \tag{76}$$

Using the method of matched asymptotic expansions described in Sec. I for Eq. (73), one obtains the asymptotics of the pyramidal slope for $0 < \varepsilon \ll 1$. In particular, the corrected edge slope A is

$$|A| = \frac{1}{\sqrt{1+b}} \left[1 - \left(\frac{\varepsilon}{1+b} \right)^{1/3} 2^{-5/6} \right] + O(\varepsilon^{2/3}). \tag{77}$$

B. Periodic pyramidal structures

For the case $b=0$, Eq. (11) can be rewritten as

$$h_t = \nabla^2(\nabla^2 h + \nabla^4 h - 3h_x^2 h_{xx} - 3h_y^2 h_{yy}) + \frac{\varepsilon}{2}(h_x^2 + h_y^2). \tag{78}$$

In this case, one can look for a solution in the form

$$h(x,y,t) = f(x) + g(y) + \varepsilon v t. \tag{79}$$

Thus, for the function $f(x)$ [and similarly for $g(y)$], one obtains

$$[f_{xxx} + f_x - (f_x)^3]_{xxx} + \frac{\varepsilon}{2}(f_x - v) = 0. \tag{80}$$

Replacing f_x by u one gets

$$(u_{xx} + u - u^3)_{xxx} + \frac{\varepsilon}{2}(u^2 - v) = 0. \tag{81}$$

This equation coincides with Eq. (14), where $v = A^2$. Thus, the problem of finding a two-dimensional (2D) periodic solution is reduced to the 1D problem considered in Sec. III. Using the method of matched asymptotic expansion we construct periodic solution with period $2L$ of Eq. (81) on the interval $(-L, L)$. As a result we obtain solution of Eq. (78) as a double-periodic function consisting of square pyramids. Example of such pyramid is shown in Fig. 12.

C. Selection of pyramid orientation

We have so far considered solutions of Eq. (11) in the form of pyramids with a particular orientation. At the same time, since the rotations by 45° transform Eq. (8) into the same equation with different coefficients, solutions of Eqs. (8) and (11) in the form of pyramids with the orientation rotated by 45° also exist. It is convenient to consider the selection of pyramid orientation using Eq. (8). One can see that if $h(x,y,\alpha,\beta)$ is the solution of Eq. (8), then the rotated

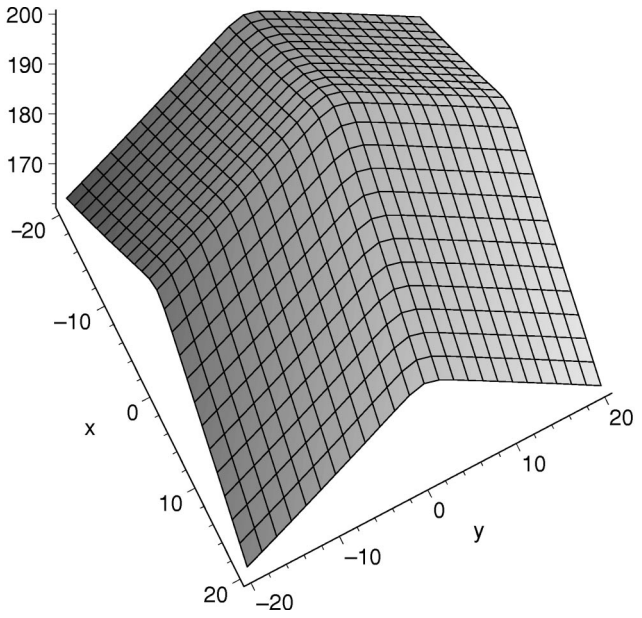

FIG. 12. One pyramid from a double-periodic system of pyramids described by Eqs. (79) and (80) for $L=200$ and $\varepsilon=0.001$.

pyramid, $h(\xi,\eta,\tilde{\alpha},\tilde{\beta})$ is also a solution, where $\xi=(x+y)/\sqrt{2}$, $\eta=(x-y)/\sqrt{2}$, $\tilde{\alpha}=(\alpha+3\beta)/2$, $\tilde{\beta}=(\alpha-\beta)/2$. In particular, if $A(\alpha,\beta)$ is the slope of the pyramid face far from the vertex where $h \sim A(x+y)$, then the face of the rotated pyramid far from its vertex will be given by $h \sim \tilde{A}(\xi+\eta)=\sqrt{2}\tilde{A}x$, where $\tilde{A}=A(\tilde{\alpha},\tilde{\beta})$; other faces are obtained by the transformations $x \to -x$, $y \to -y$, $x \to y$. Take for simplicity $m=\delta=1$ and $F=0$ in Eq. (8) to obtain for A and $\tilde{A}$

$$A^2 = \frac{1}{\alpha/3+\beta}, \quad \tilde{A}^2 = \frac{3}{2\alpha}. \tag{82}$$

It is natural to assume that the selected orientation will be that for which the Lyapunov functional density Φ defined in Eq. (7) will have the smaller value. Neglecting the energies of edges and vertices and taking into account the energies of the planar faces only (which is justified for large enough pyramids) one obtains for pyramids with different orientations, whose faces are described by $h_\diamond \sim A\{(x+y), (x-y), (y-x), (-x-y)\}$ and $h_\square \sim \tilde{A}\sqrt{2}\{x,-x,y,-y\}$,

$$\Phi_\diamond = -8A^2 + \left(\frac{2}{3}\alpha + 2\beta \right) A^4,$$
$$\Phi_\square = -8\tilde{A}^2 + \frac{4}{3}\alpha\tilde{A}^4. \tag{83}$$

Using Eq. (82) and (83), one can easily see that

$$\Phi_\diamond < \Phi_\square \quad \text{for} \quad 0 < \beta < \frac{\alpha}{3}, \quad \diamond \text{ pyramids selected,}$$

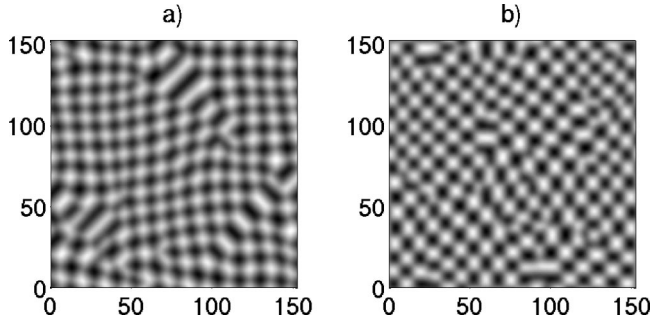

FIG. 13. Pyramids with different orientations: numerical solutions of Eq. (11) for $D=0$ and (a) $b=0$, (b) $b=2$.

$$\Phi_{\diamond} > \Phi_{\square} \quad \text{for } \frac{\alpha}{3} < \beta < \alpha, \quad \square \text{ pyramids selected,} \tag{84}$$

and $\Phi_{\diamond} = \Phi_{\square}$ for $\beta = \alpha/3$ when $A = \tilde{A}$; note that in this case Φ, together with Eq. (8), becomes isotropic.

Another selection criterion for pyramid orientation for $D=0$ can be obtained from the linear stability analysis of the pyramid faces far from the vertex. In the case of a ''diamond'' pyramid, with the asymptotic shape of the face far from the vertex, $h \sim A(x+y)$, for the perturbations of the face shape $\sim e^{\sigma t + i\mathbf{k}\cdot\mathbf{r}}$, one obtains the following dispersion relation:

$$\sigma = -k^6 + k^2 Q(k_x, k_y), \tag{85}$$

where

$$Q(k_x, k_y) = (k_x^2 + k_y^2)[1 - A^2(\alpha+\beta)] - 4\beta A^2 k_x k_y . \tag{86}$$

According to Eq. (85) the pyramid face far from the vertex is stable when the quadratic form (86) is negative definite, i.e., if and only if the following two inequalities hold:

$$A^2 > \frac{1}{\alpha - \beta}, \tag{87}$$

$$\alpha - \beta > 0. \tag{88}$$

Using Eq. (82) one finds that the faces of the diamond pyramids far from the vertex are stable for $0 < \beta < \alpha/3$. Similarly, one finds that the faces of the ''box'' pyramids are stable for $\alpha/3 < \beta < \alpha$. One can see that the linear stability criteria for the faces of differently oriented pyramids coincide with the energetic criteria (84).

For the rescaled Eq. (11), the selection criterion becomes very simple: diamond pyramids are selected for $0 < b < 1$, while the box pyramids are selected for $1 < b < 3$. Figure 13 shows the results of the numerical solution of Eq. (11) for $D=0$, by means of a pseudospectral method with periodic boundary conditions, for two cases: $b=0$ and $b=2$. One can clearly see the selection of differently oriented pyramids. Figure 13 shows the pyramidal structures shortly after their formation. The structures will undergo further coarsening, which is discussed in the following section.

D. Effect of the growth rate and pyramid stability

As in $1+1$ case, the slope of the pyramids in $2+1$ case depends on the growth rate D. The increase of the growth rate leads to the decrease of the pyramid slope so that after D exceeds a certain threshold the slope decreases below the spinodal value and the pyramid becomes unstable. The critical value of D can be estimated using the asymptotics for the pyramid slope (77) and the asymptotic shape of the pyramid face far from the vertex, $h \sim A(D)(x+y)$. For the perturbations of the face shape $\sim e^{\sigma t + i\mathbf{k}\cdot\mathbf{r}}$, one obtains the following dispersion relation:

$$\sigma = -k^6 + k^2 Q_D(k_x, k_y) + iDA(D)(k_x + k_y), \tag{89}$$

where

$$Q_D(k_x, k_y) = (k_x^2 + k_y^2)[1 - A^2(D)(3+b)] - 4bA^2(D)k_x k_y . \tag{90}$$

Simple linear analysis similar to that described above shows that the pyramid face far from the vertex is stable if and only if the following two inequalities hold:

$$A^2(D) > \frac{1}{3-b}, \qquad 3 - b > 0. \tag{91}$$

Using the asymptotic expression (77) for the pyramid slope for the case $D \sim \epsilon \ll 1$, one obtains the following restriction for the growth rate at which the pyramid structures are stable:

$$D < 2^{5/2}(1+b)\left(1 - \sqrt{\frac{1+b}{3-b}}\right)^3, \quad 0 < b < 1. \tag{92}$$

Condition (92) is derived for the stability of diamond pyramids. Similarly, one obtains that box pyramids are stable for

$$D < 2^{7/2}\left(1 - \frac{1}{\sqrt{b}}\right)^3, \quad 1 < b < 3. \tag{93}$$

One can see from conditions (92) and (93) that the face of a pyramid far from the vertex is stable only for deposition rates smaller than the critical value which depends on the anisotropy coefficient b. For $b=0$ condition (92) gives $D < 0.43$ that corresponds to the one-term approximation of $1+1$ case considered in Sec. III. Since the stability condition (92) is based on the asymptotic formula for small D it should be considered as an estimate for the critical deposition rate at which pyramid faces far from the vertex become unstable. Above this critical value of D, one cannot expect the coarsening of the pyramids to proceed indefinitely since the large pyramids are unstable. In this case another spatiotemporal dynamics is observed which is discussed below.

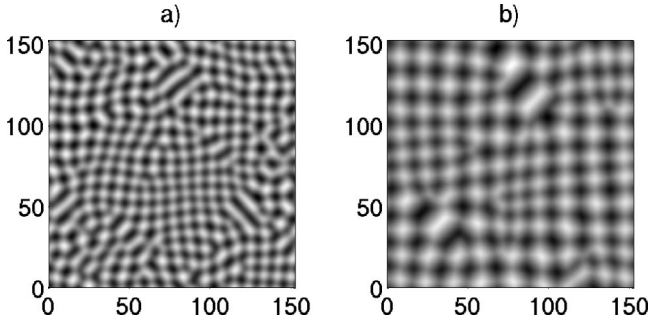

FIG. 14. Surface pyramidal structures in the case of pure faceting without growth—numerical solutions of Eq. (11) with $a=b=0$ and $D=0.0$ right after the structure formation (a) and at the late stage of coarsening (b).

E. Dynamics of pyramidal structures

1. Pyramids and antipyramids

In order to study the dynamics of pyramidal structures described by Eq. (11) we solved this equation numerically, by means of a pseudospectral code for various values of the deposition rate D in a square domain with the side $L=40\pi$. For zero and small deposition rates, the pyramidal structure undergoes further coarsening so that the lateral size and the height of the pyramids grow in time in such a way that the pyramid slope remains the same. Figure 14 shows typical pyramidal patterns observed for $D=0$ when there is no deposition, just pure faceting of a thermodynamically unstable crystal surface by the surface-diffusion mechanism. The two figures correspond to two different moments of time: right after the formation of the pyramidal structure [Fig. 14(a)] and at the late stage of the coarsening process [Fig. 14(b)]. The important feature of the pyramidal structure in the absence of deposition ($D=0$) is that the pyramids and pits (''antipyramids'') are equivalent. This is because for $D=0$, Eq. (11) is symmetric with respect to transformation $h\rightarrow -h$. However, a nonzero deposition rate, $D>0$, breaks this symmetry and results in the growth of pyramids and disappearance of antipyramids. Indeed, as follows from the dispersion relation (85), perturbations of a pyramid shape are convectively transported downhill into pits (antipyramids) making them gradually disappear. This can be seen in Fig. 15

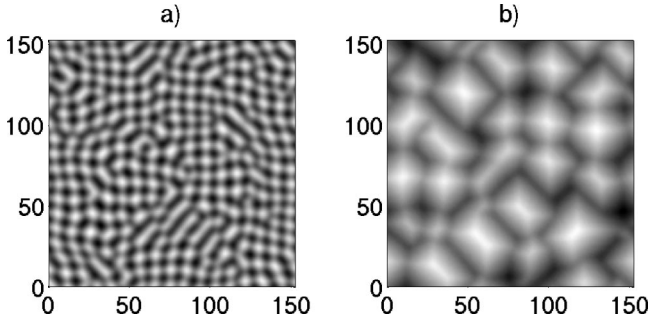

FIG. 15. Surface pyramidal structures in the case of pure faceting without growth—numerical solutions of Eq. (11) with $a=b=0$ and $D=0.01$ right after the structure formation (a) and at the late stage of coarsening (b).

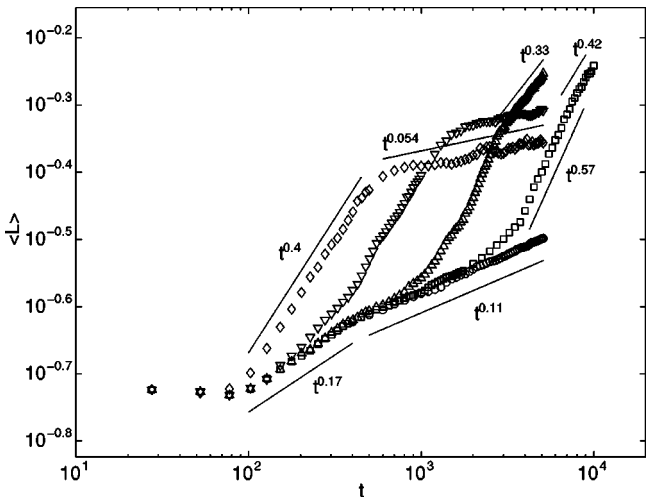

FIG. 16. Coarsening kinetics of pyramidal structures for various values of the deposition rate: ○, $D=0.0$; □, $D=0.01$; △, $D=0.02$; ▽, $D=0.05$; ◇, $D=0.1$.

that shows typical pyramidal structures for a small deposition rate, $D=0.01$, shortly after the structure formation [Fig. 15(a)] and long time after it [Fig. 15(b)]. One can see that antipyramids have disappeared so that only pyramids divided by valleys are finally left. Note that in the case of etching ($D<0$), the effect of the symmetry breaking will be the opposite: the antipyramids will survive while the pyramids will disappear.

2. Coarsening and roughening

The dynamics of the pyramidal structures after their formation strongly depends on the deposition rate D and is somewhat similar to the dynamics observed in the case of a $1+1$ model. The coarsening dynamics is shown in Fig. 16 where the mean spatial scale of the pyramidal structures, $\langle L\rangle$, is shown for different values of D, averaged over ten random initial data for each value of D. The mean spatial scale was computed as $\langle L\rangle=(\langle L_x\rangle+\langle L_y\rangle)/2$, where $\langle L_x\rangle$ and $\langle L_y\rangle$ are the mean scales in x and y directions, respectively; $\langle L_x\rangle$ and $\langle L_y\rangle$ are defined as $\langle L_x\rangle=\Sigma_y L_0/N_x^y$ and $\langle L_y\rangle=\Sigma_x L_0/N_y^x$, where L_0 is the size of the square computational domain, N_x^y (N_y^x) is the number of zeros of h_x (h_y) in a fixed y (x) layer, and the summation is over all y (x) layers.

When there is no deposition, $D=0$, there is pure faceting, and we have observed a rather slow coarsening of the pyramidal structures. One can clearly see two stages. First, one observes the power-law coarsening $\langle L\rangle\sim t^{0.17}$. Then there is a crossover to even slower coarsening, $\langle L\rangle\sim t^{0.11}$. The exponent of the first stage is very close to 1/6. This can be understood from the balance of several simultaneous processes described by Eq. (11). Indeed, after the pyramidal structure has been formed, the linear term describing the spinodal instability of the surface, $\nabla^4 h$, is balanced by the nonlinear anisotropic stabilization terms, so that if L is a characteristic width of the pyramid and H is its characteristic height then $HL^{-4}\sim H^3L^{-6}$ and therefore $H\sim L$, which means that the slope of pyramids remains unchanged during the coarsening,

and this is what is observed. Thus, the coarsening dynamics is driven by the balance of the two terms, the rate of change, h_t, and the regularization, $\nabla^6 h$, describing the additional energy of edges and corners. If a characteristic time scale is T then the balance between the two terms gives $HT^{-1} \sim HL^{-6}$ from which one obtains $L \sim T^{1/6}$. These estimates are valid, however, when the width of the edges are not very small in comparison with the width of the pyramids [22]. Also, since the duration of this coarsening stage is only several times more than the characteristic time of the formation of the pyramidal structure this power law should be considered as an intermediate asymptotics which is not associated with long-time scale-invariant behavior. With further pyramid growth, when the width of edges becomes much smaller than the characteristic pyramid scale, the estimate $\nabla^6 h \sim HL^{-6}$ is no longer valid and the coarsening rate is governed by a complicated dynamics of the web of edges and valleys [5,25]. At this stage, the crossover to the slower coarsening occurs. The slow coarsening stage starts long after the characteristic time of the pyramidal structure formation and the power-law kinetics can be associated with the scale-invariant behavior. Presumably, a detailed consideration of the dynamics of the web of edges similar to that considered in Refs. [5,25] could explain the crossover to a slower coarsening and the small coarsening exponent, but this is beyond the scope of the present paper.

In the presence of even small deposition, the coarsening dynamics drastically changes. Typical examples are shown in Fig. 16 for $D=0.01$ and $D=0.02$. One can clearly see several stages. At the first two stages, the coarsening dynamics is the same as in the case without deposition: one can see a slow coarsening, $\sim t^{0.17}$, with the later crossover to the even slower coarsening, $\sim t^{0.11}$. At this stage, the convective term $\frac{1}{2}D|\nabla h|^2$ is small and does not affect the pyramidal structure which at this stage looks like those shown in Figs. 14(a) and 15(a), and exhibits the symmetry between pyramids and antipyramids. However, with further growth, the convective term becomes larger and breaks the symmetry between pyramids and antipyramids, which corresponds to a transitional stage showing an accelerated coarsening. Finally, when antipyramids disappear, so that the surface structure exhibits only pyramids divided by narrow valleys, the stage of fast coarsening takes over, at which we observe $\langle L \rangle \sim t^{0.57}$. Similar behavior, exhibiting a crossover from a slow to a fast coarsening in the presence of the KPZ-type nonlinear term breaking $h \to -h$ symmetry was observed and discussed in Ref. [12]. According to Ref. [12], in the presence of this nonlinear term, the faces of the pyramids with a nonzero slope grow faster than valleys whose average slope is zero (or very small). Since the characteristic width of valleys is $O(1)$ and the spatial fraction of the surrounding valleys is larger for small pyramids than for large ones, the effective growth rate of small pyramids is smaller than that of large pyramids which leads to preferential coalescence of small pyramids and to the coarsening rate $\sim t^{0.5}$ (see Ref. [12] for detailed explanation). It is interesting that in our system, the fast coarsening stage exhibits further crossover to a slower (but still relatively fast) regime at long times, $\sim t^{0.42}$ for $D=0.01$, and $\sim t^{0.33}$ for $D=0.02$. The origin of this regime as well as for how long it lasts is as yet unknown.

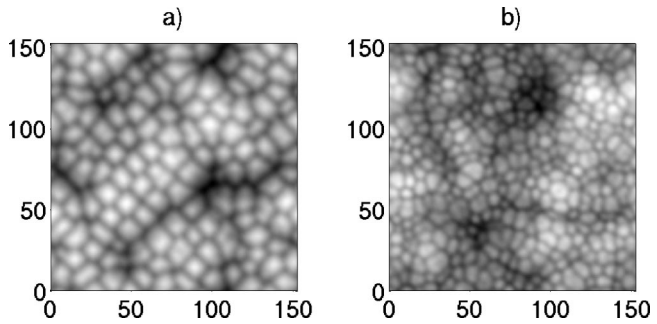

FIG. 17. Surface structures described by solutions of Eq. (11) with $a=b=0$ and (a) $D=0.5$, (b) $D=10.0$.

With the increase of the deposition rate, the initial slow stage of coarsening disappears and the fast coarsening starts right after the formation of the initial pyramidal structure in which the pyramid-antipyramid symmetry is already broken. In this case, one observes a relatively long stage of fast coarsening, $\sim t^{0.4}$, that, however, stops after some time and becomes extremely slow, $\sim t^{0.054}$. Examples are shown in Fig. 16 for $D=0.05$ and $D=0.1$. Since the fast coarsening stage starts right after the formation of the pyramidal structure, its power-law kinetics should be considered as an intermediate asymptotics rather than a scale-invariant long-time behavior.

With further increase of the deposition rate D, the fast coarsening stage becomes shorter so that a pyramidal structure with a certain scale is established, which does not coarsen in time but undergoes a slow chaotic spatiotemporal dynamics. In this structure, which is shown in Fig. 17(a), a fourfold symmetry of the [001] surface is still present. However, for larger D the symmetry disappears and the surface exhibits chaotic spatiotemporal dynamics of splitting and merging isotropic mounds, shown in Fig. 17(b), which is typical of 2D Kuramoto-Sivashinsky equation [18]. Indeed, similar to what has been discussed in $1+1$ case, in $2+1$ case, by changing $h \to h/D$ and taking $D \to \infty$, Eq. (11) is also transformed into an isotropic, Kuramoto-Sivashinsky-type 2D equation with a higher-order linear operator,

$$h_t - \frac{1}{2}|\nabla h|^2 - \nabla^4 h - \nabla^6 h = 0. \tag{94}$$

Equation (94) is rotationally invariant and the surface described by Eq. (94) looks rough. We have not studied the roughening characteristics in this limiting case and postpone it to future investigation. Note that the roughening properties of a 2D KS equation are still under discussion [18].

ACKNOWLEDGMENTS

This research was supported by the National Science Foundation, Grant No. 0102794, and by the U.S.–Israel Binational Science Foundation, Grant No. 9800086.

[1] V.A. Shchukin and D. Bimberg, Rev. Mod. Phys. **71**, 1125 (1999).
[2] B.J. Spencer, P.W. Voorhees, and S.H. Davis, Phys. Rev. Lett. **67**, 3696 (1991).
[3] Y.W. Zhang, Phys. Rev. B **61**, 10 388 (2000).
[4] M. Siegert and M. Plischke, Phys. Rev. Lett. **73**, 1517 (1994).
[5] M. Siegert, Phys. Rev. Lett. **81**, 5481 (1998).
[6] J. Stewart and N. Goldenfeld, Phys. Rev. A **46**, 6505 (1992).
[7] F. Liu and H. Metiu, Phys. Rev. B **48**, 5808 (1993).
[8] M.E. Gurtin, *Thermomechanics of Evolving Phase Boundaries in the Plane* (Clarendon Press, Oxford, 1993).
[9] A.A. Golovin, S.H. Davis, and A.A. Nepomnyashchy, Phys. Rev. E **59**, 803 (1999).
[10] A.A. Golovin, S.H. Davis, and A.A. Nepomnyashchy, Physica D **122**, 202 (1998).
[11] A.A. Golovin, A.A. Nepomnyashchy, S.H. Davis, and M.A. Zaks, Phys. Rev. Lett. **86**, 1550 (2001).
[12] P. Smilauer, M. Rost, and J. Krug, Phys. Rev. E **59**, R6263 (1999).
[13] W.W. Mullins, J. Appl. Phys. **28**, 333 (1957).
[14] W.W. Mullins, Metall. Mater. Trans. A **26A**, 1917 (1995).
[15] J.W. Cahn and J.E. Taylor, Acta Metall. Mater. **42**, 1045 (1994).
[16] M. Kardar, G. Parisi, and Y.C. Zhang, Phys. Rev. Lett. **56**, 889 (1986).
[17] C.L. Emmott and A.J. Bray, Phys. Rev. E **54**, 4568 (1996).
[18] T. Bohr, M.H. Jensen, G. Paladin, and A. Vulpiani, *Dynamical Systems Approach to Turbulence* (Cambridge University Press, Cambridge, London, 1998).
[19] J. Krug, Adv. Phys. **46**, 139 (1997).
[20] A. Pimpinelli and J. Villain, *Physics of Crystal Growth* (Cambridge University Press, Cambridge, London, 1998).
[21] V. Yakhot, Phys. Rev. A **24**, 642 (1981).
[22] There are other models as well as experimental observations that give the same exponent, 1/6, see, e.g., Refs. [23,24], and references therein.
[23] M. Papoular, Europhys. Lett. **33**, 221 (1996).
[24] S. Song, M. Yoon, S.G.J. Mochrie, G.B. Stephenson, and S.T. Milner, Surf. Sci. **372**, 37 (1997).
[25] D. Moldovan and L. Golubovic, Phys. Rev. E **61**, 6190 (2000).